Interpretation of optical three-dimensional coherent spectroscopy

Michael Titze and Hebin Li

Interpretation of Optical Three-dimensional Coherent Spectroscopy

Michael Titze and Hebin Li*

Department of Physics, Florida International University, Miami, Florida 33199

(Dated: August 23, 2017)

As an extension to powerful Two-Dimensional Coherent Spectroscopy (2DCS), optical Three-Dimensional Coherent Spectroscopy (3DCS) has been experimentally implemented and found beneficial in studying various systems in physics and chemistry. A critical challenge is how to interpret 3D spectra and extract useful quantitative information, given the richness and complexity of 3D data. Here, we demonstrate how the information of a system's optical response is manifested in 3D spectra by theoretical simulations of a few representative examples including a homogeneous three-level V system, an inhomogeneous three-level V system, and an inhomogeneous three-level ladder system. These examples show that important parameters of the system can be extracted from the spectral pattern, peak positions, amplitudes, and line shapes. The method developed here can be used to analyze 3D spectra of more sophisticated systems which might be a generalization or combination of the three examples, contributing to develop a general approach for the interpretation of 3D spectra.

I. INTRODUCTION

Optical Multidimensional Coherent Spectroscopy (MDCS) [1] has been a major advance in ultrafast spectroscopy. The concept of multidimensional spectroscopy was originally developed in nuclear magnetic resonance [2]. The idea has been realized in the optical region in the past two decades. The most common implementation is Two-Dimensional Coherent Spectroscopy (2DCS) [3] in which the spectrum is presented with two frequency axes. By unfolding a spectrum onto a two-dimensional (2D) plane, 2DCS can better separate different contributions from various processes in the system. This leads to many advantages of 2DCS over conventional one-dimensional (1D) spectroscopy [3, 4]. For example, one can identify the inhomogeneous broadening and extract both the homogeneous and inhomogeneous linewidths in a single 2D spectrum [5], and various interactions and couplings can be identified and characterized in 2D spectra. These unique capabilities of 2DCS have made it a powerful tool to study structure and dynamics in various systems. A few examples include the studies of structural information in proteins [6], hydrogen-bond dynamics in water [7], energy transfer in photosynthetic complex [8–10], dipole-dipole interactions in atomic vapors [11, 12], and many-body dynamics in semiconductor quantum wells [13–17] and dots [18–21].

In many cases, the spectral contributions from different processes are not completely separated in a 2D spectrum. The next step is to extend the technique into a third dimension for Three-Dimensional Coherent Spectroscopy (3DCS). By further unfolding the spectrum in a three-dimensional (3D) space, 3DCS improves the existing capabilities of 2DCS and also introduces new ones that cannot be realized in 2DCS. It is worthwhile to note that adding a third dimension is not merely a different

way to plot 2D spectral data. A 3D coherent spectrum is different from simply taking a series of 2D spectra as a function of time and taking a Fourier transform. To construct a 3D coherent spectrum, the third time delay is scanned with all excitation pulses phase locked to preserve the coherence and phase information in the third dimension. This is similar to the argument made for constructing a 2D spectrum from phase-stabilized 1D measurements.

A number of different approaches have been implemented to perform 3DCS for different goals [22]. Early 3DCS experiments [23–27] were based on the fifth order nonlinear response of a sample to five excitation fields. However, 3DCS on electronic transitions has been mainly focused on the third order nonlinear response, with the objective to obtain more complete information about the electronic transitions. For example, the technique has revealed the double-quantum coherence in a quantum well [28], the coupling between two adjacent quantum wells [29], and the Hamiltonian of an atomic vapor [30] and light harvesting materials [31]. Although these experiments were realized in the time domain with femtosecond lasers, it is also possible to implement 3DCS with a frequency domain approach [32]. In this article, we focus our discussion on 3DCS based on a time domain approach.

A critical challenge in 3DCS is the interpretation of 3D spectra. What kind of information about the system's optical nonlinear response can be extracted from the spectral pattern, peak positions, peak amplitudes and lineshapes? How to extract such information from experimental spectra? Which information is difficult or impossible to obtain in 2DCS but accessible or easier to obtain in 3DCS? The answers to these important questions are essential for the efficient use of 3DCS and identifying objectives that can benefit from using 3DCS. Here we are not trying to provide answers to these questions in all scenarios, which will be research topics in specific fields of using 3DCS. Instead, we approach the problem with a few representative examples to demonstrate how dif-

*hebin.li@fiu.edu

ferent 3D spectral features are associated with different parameters of the system's optical nonlinear response. The methods used on these examples can be extended to interpret 3D spectra of other systems which might be an extension or combination of the examples here.

This article is organized as the following. Section II briefly introduces the specific experimental implementation that the subsequent discussion is based on. Section III gives a general theoretical description based on the optical Bloch equation. In Section IV, a 3D spectrum of a three-level V system is simulated and discussed. In Section V, the effects of inhomogeneous broadening in 3D spectra are demonstrated and discussed. Section VI applies the same analysis to a different system, that is a three-level ladder scheme. A summary is presented at the end.

II. IMPLEMENTATION OF 3D COHERENT SPECTROSCOPY

We consider the implementation of 3D coherent spectroscopy based on a three-pulse transient four-wave mixing (TFWM) experiment in the box geometry. As shown in Fig. 1(a), three phased-locked femtosecond pulses, A, B, and C, with wave vectors, $\mathbf{k}_A$, $\mathbf{k}_B$, and $\mathbf{k}_C$, respectively, are arranged in the box geometry. The three pulses mix in the sample to produce a nonlinear TFWM signal in the phase matching direction, $\mathbf{k}_S = -\mathbf{k}_A + \mathbf{k}_B + \mathbf{k}_C$. The excitation pulses arrive at the sample in a sequence. The so called rephasing time ordering is shown in Fig. 1(b) where the delay between the first and second pulses is τ, the delay between the second and third pulses is T, and the emission time is t. The TFWM signal is generated by the third-order polarization

$$P^{(3)}_{FWM}(\mathbf{r},\tau,T,t) = \int_0^\infty \int_0^\infty \int_0^\infty dt'_A dt'_B dt'_C \cdot \mathcal{R}^{(3)}_{E_A E_B E_C}$$
$$E_A(\mathbf{r},t'_A - t_1) E_B(\mathbf{r},t'_B - t_2) E_C(\mathbf{r},t'_C - t_3), \quad (1)$$

where $\mathcal{R}^{(3)}_{E_A E_B E_C}$ is the third-order time-dependent response function of the system. The electric field of each pulse is given by $E_j(\mathbf{r},t) = \widetilde{\mathcal{E}}_j(t) \cdot e^{i(\mathbf{k}_j \cdot \mathbf{r} - \omega_j t)} + c.c.$, where $j = A, B, C$ and the slowly varying amplitude $\widetilde{\mathcal{E}}_j$ defines the time-domain pulse shape. The three pulses A, B, and C arrive at the sample at the times t_1, t_2, and t_3, respectively. The emitted TFWM electric field is

$$E_{FWM} \propto i\omega P^{(3)}_{FWM} \quad (2)$$

with ω being the emission frequency. The general expression of Eq. (1) includes the signals in all phase-matching directions ($\pm\mathbf{k}_A \pm \mathbf{k}_B \pm \mathbf{k}_C$). Here we consider only one phase-matching direction $\mathbf{k}_S$, thus only the terms contributing to the signal in the direction $\mathbf{k}_S$ will be accounted for in the calculation.
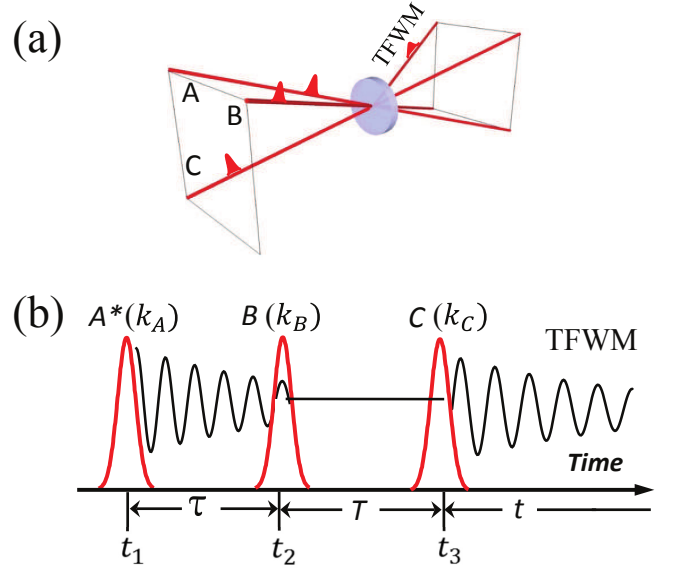

FIG. 1: (a) The box geometry in which three excitation pulses are aligned to three corners of a box and the signal emits at the forth corner. (b) The time ordering of the excitation pulses in the so-called rephasing excitation sequence.

During the experiment, the TFWM signal E_{FWM} is measured through spectra interferometry by using another phase-locked pulse E_R as a reference pulse. Specifically, the combined signal of TFWM and reference pulse is recorded by a spectrometer as an interferogram

$$I_{SI} = |E_{FWM} + E_R|^2$$
$$= |E_{FWM}|^2 + |E_R|^2 + E_{FWM}E_R^* + E_{FWM}^* E_R. \,(3)$$

The individual spectra of the TFWM signal $I_{FWM} = |E_{FWM}|^2$ and the reference $I_R = |E_R|^2$ are also recorded separately. To extract the TFWM signal field, we first subtract the background from the interferogram ($I_{SI} - I_{FWM} - I_R$), leaving only the interference terms. The term $E_{FWM}E_R^*$ can be isolated in the frequency domain using a Fourier filter. The magnitude of E_R can be determined from the reference spectrum I_R. The time delay and relative phase between the TFWM signal and the reference pulse can be characterized in the experiment [33, 34]. Thus, the TFWM signal field can be obtained by dividing the interference term with the reference pulse field E_R. The experimentally measured signal field E_{FWM} is related to the third-order polarization $P^{(3)}_{FWM}$, which is the calculated quantity in the following calculations, through Eq. (2). We note that the sample here is considered optically thin, in which case the spectral distortion due to pulse propagation effects [35, 36] is negligible.

The measurements are repeated as the delay times τ and T are scanned systematically. In the time domain, the recorded signal $S(\tau, T, t)$ is a function of three delay times. A 3D spectrum $S(\omega_\tau, \omega_T, \omega_t)$ can be constructed by Fourier transforming the time-domain signal with re-

spect to the delay times.

III. THIRD-ORDER NONLINEAR RESPONSE TO OPTICAL EXCITATIONS

Based on the density matrix formalism, the light-matter interaction can be described by the equation of motion [37].

$$\dot{\rho} = -\frac{i}{\hbar}[H,\rho] - \frac{1}{2}\{\Gamma,\rho\}, \qquad (4)$$

where $H = H_0 + H_I$, $[H,\rho] = H\rho - \rho H$ and $\{\Gamma,\rho\} = \Gamma\rho + \rho\Gamma$. The matrix elements of H_0 and H_I are $H_{0,ij} = \hbar\omega_i\delta_{ij}$ and $H_{I,ij} = -\mu_{ij}E(t)$ ($H_{I,ij} = 0$ for $i = j$), where $\hbar\omega_i$ is the energy of state $|i\rangle$, $E(t)$ is the electric field, $\mu_{ij}(i \neq j)$ is the dipole moment of the transition between states $|i\rangle$ and $|j\rangle$, and δ_{ij} is the Kronecker delta function. The relaxation operator Γ has matrix elements $\Gamma_{ij} = \frac{1}{2}(\gamma_i + \gamma_j)$, where γ_i and γ_j are the population decay rates. In general, coherences can decay due to pure dephasing processes in addition to population decay. To include pure dephasing, the equation of motion can be modified as

$$\dot{\rho}_{ij} = -\frac{i}{\hbar}\sum_k (H_{ik}\rho_{kj} - \rho_{ik}H_{kj}) - \Gamma_{ij}\rho_{ij}. \qquad (5)$$

The relaxation operator Γ is redefined to have matrix elements $\Gamma_{ij} = \frac{1}{2}(\gamma_i + \gamma_j) + \gamma_{ij}^{ph}$, where γ_{ij}^{ph} is the pure coherence dephasing rate ($\gamma_{ij}^{ph} = 0$ for $i = j$).

To calculate the third-order nonlinear response of the medium, the equation of motion can be solved perturbatively for $\rho_{ij}^{(3)}$. The polarization is then given by $P_{ij}^{(3)} = N\mu_{ij}\rho_{ij}e^{i\omega t}$, where N is the number density. In general, the third-order nonlinear response, $\rho_{ij}^{(3)}$, consists of multiple terms contributed by different quantum pathways. The calculation can be aided with double-sided Feynman diagrams so that the contribution from each single pathway is calculated separately.

IV. 3D SPECTRUM OF A THREE-LEVEL V SYSTEM

To demonstrate 3DCS, we choose a model system with a three-level V energy scheme, as shown in Fig. 2(a), which is appropriately simple and yet sufficiently complex to demonstrate the unique capabilities of 3DCS. The results can be generalized to systems with multiple excited and/or ground states.

A. Excitation pathways and corresponding third-order responses

Considering the excitation by the pulse sequence shown in Fig. 1(b) and assuming that the laser band-
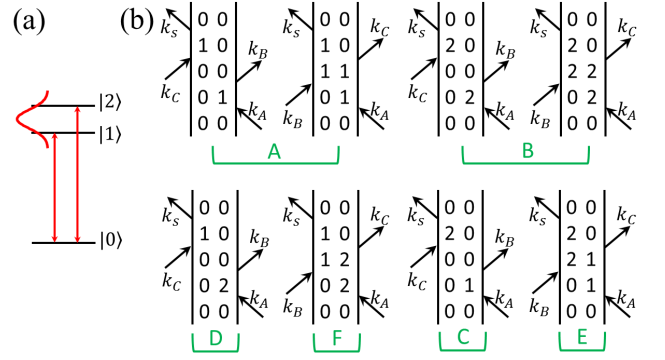

FIG. 2: (a) The energy-level diagram for a three-level V system. (b) Double-sided Feynman diagrams representing 8 possible excitation quantum pathways in the experiment.

TABLE I: The frequency coordinates of each spectral peak in the 3D spectrum.

Group	Frequency Coordinates		
	ω_τ	ω_t	ω_T
A	$-\omega_{10}$	ω_{10}	0
B	$-\omega_{20}$	ω_{20}	0
C	$-\omega_{10}$	ω_{20}	0
D	$-\omega_{20}$	ω_{10}	0
E	$-\omega_{10}$	ω_{20}	ω_{21}
F	$-\omega_{20}$	ω_{10}	ω_{12}

width covers both excited states $|1\rangle$ and $|2\rangle$, the third-order TFWM signal in the phase matching direction $\mathbf{k}_S$ includes contributions from eight excitation pathways that are represented by the double-sided Feynman diagrams shown in Fig. 2(b). The eight pathways can be divided into six different groups labeled A through E. The two pathways in group A have an absorption frequency of $\omega_\tau = -\omega_{10}$, an emission frequency of $\omega_t = \omega_{10}$, and a mixing frequency of $\omega_T = 0$, resulting in a spectral peak at $(\omega_\tau = -\omega_{10}, \omega_t = \omega_{10}, \omega_T = 0)$ in the 3D spectrum. Similarly, the pathways in other groups lead to spectral peaks at different locations in the 3D spectrum. The specific frequency coordinates for the spectral peak associated with each group of pathways are listed in Table I. The absorption frequency has negative values since the excitation pulse A is conjugated in the current configuration.

The third-order nonlinear response is calculated separately for each pathway represented by a double-side Feynman diagram (see the Appendix for details). For the first diagram in group A, we have

$$\rho^{(3)}_{10,A1} =$$

$$\frac{i\mu_{10}}{2\hbar}e^{i\mathbf{k}_C\cdot\mathbf{r}}\int_{-\infty}^{t}dt'''e^{-i(\omega_{10}-i\Gamma_{10})(t-t''')}\widetilde{\mathcal{E}}_C(t''')e^{-i\omega t'''}$$

$$\frac{-i\mu_{10}}{2\hbar}e^{i\mathbf{k}_B\cdot\mathbf{r}}\int_{-\infty}^{t_3}dt''e^{-\Gamma_{00}(t_3-t'')}\widetilde{\mathcal{E}}_B(t'')e^{-i\omega t''}$$

$$\frac{-i\mu_{10}}{2\hbar}e^{-i\mathbf{k}_A\cdot\mathbf{r}}\int_{-\infty}^{t_2}dt'e^{-i(\omega_{01}-i\Gamma_{10})(t_2-t')}\widetilde{\mathcal{E}}_A^*(t')e^{i\omega t'}\rho^{(0)}_{00},$$

$$(6)$$

where ω is the carrier frequency of all pulses, and t_1, t_2, and t_3 are the arrival times for pulses A, B, and C, respectively. The system is initially in the ground state, that is $\rho^{(0)}_{00} = 1$. For the cases where the pulse duration is much shorter than the characteristic time scale of the dynamics, the excitation pulse can be approximated with a Dirac delta function such that $\widetilde{\mathcal{E}}_{A,B,C} = \mathcal{E}_{A,B,C}\delta(t - t_{1,2,3})$, where $\mathcal{E}_{A,B,C}$ represents the amplitude of the pulse. Then equation (6) can be rewritten as

$$\rho^{(3)}_{10,A1} = \frac{-i\mu_{10}^3}{8\hbar^3}e^{i(-\mathbf{k}_A+\mathbf{k}_B+\mathbf{k}_C)\cdot\mathbf{r}}\mathcal{E}_A^*\mathcal{E}_B\mathcal{E}_C$$

$$\int_{-\infty}^{t}dt'''e^{-i(\omega_{10}-i\Gamma_{10})(t-t''')}\delta(t'''-t_3)e^{-i\omega t'''}$$

$$\int_{-\infty}^{t_3}dt''e^{-\Gamma_{00}(t_3-t'')}\delta(t''-t_2)e^{-i\omega t''}$$

$$\int_{-\infty}^{t_2}dt'e^{-i(\omega_{01}-i\Gamma_{10})(t_2-t')}\delta(t'-t_1)e^{i\omega t'}$$

$$= \frac{-i\mu_{10}^3}{8\hbar^3}e^{i\mathbf{k}_S\cdot\mathbf{r}}\mathcal{E}_A^*\mathcal{E}_B\mathcal{E}_C e^{-\Gamma_{10}(t-t_3+t_2-t_1)}$$

$$e^{-\Gamma_{00}(t_3-t_2)}e^{-i\omega_{10}t}e^{-i(\omega-\omega_{10})(t_3+t_2-t_1)}$$

$$\Theta(t_2-t_1)\Theta(t_3-t_2)\Theta(t-t_3), \qquad (7)$$

where Θ's are heaviside step functions. We define the time intervals as $\tau = t_2 - t_1$, $T = t_3 - t_2$, and $t = t - t_3$, and assume the excitation is on resonance ($\omega - \omega_{10} = 0$). The third-order polarization is given by

$$P^{(3)}_{10,A1}(\tau,t,T) = N\mu_{10}\rho^{(3)}_{10,A1}e^{i\omega t}$$

$$= \frac{-iN\mu_{10}^4}{8\hbar^3}e^{i\mathbf{k}_S\cdot\mathbf{r}}\mathcal{E}_A^*\mathcal{E}_B\mathcal{E}_C\Theta(\tau)\Theta(T)\Theta(t)$$

$$e^{-\Gamma_{10}(t+\tau)-\Gamma_{00}T}. \qquad (8)$$

This is the time-domain solution in the rotating frame. In general, the spectrum in the time domain can be constructed by stepping the time delays τ, T, and t. The time-domain spectrum can then be numerically Fourier-transformed to obtain the frequency-domain spectrum. In the current case, the Fourier transform of Eq. (8) has

an analytical form which is given by

$$P^{(3)}_{10,A1}(\omega_\tau,\omega_t,\omega_T) = \frac{-iN\mu_{10}^4}{16\sqrt{2}\pi^{\frac{3}{2}}\hbar^3}e^{i\mathbf{k}_S\cdot\mathbf{r}}\mathcal{E}_A^*\mathcal{E}_B\mathcal{E}_C$$

$$\frac{1}{\Gamma_{10}-i(\omega_\tau+\omega_{10})}\cdot\frac{1}{\Gamma_{10}-i(\omega_t-\omega_{10})}\cdot\frac{1}{\Gamma_{00}-i\omega_T},$$

$$(9)$$

in the laboratory frame. Similarly, the third-order polarization due to the second diagram in group A is given by

$$P^{(3)}_{10,A2}(\omega_\tau,\omega_t,\omega_T) = \frac{-iN\mu_{10}^4}{16\sqrt{2}\pi^{\frac{3}{2}}\hbar^3}e^{i\mathbf{k}_S\cdot\mathbf{r}}\mathcal{E}_A^*\mathcal{E}_B\mathcal{E}_C$$

$$\frac{1}{\Gamma_{10}-i(\omega_\tau+\omega_{10})}\cdot\frac{1}{\Gamma_{10}-i(\omega_t-\omega_{10})}\cdot\frac{1}{\Gamma_{11}-i\omega_T}.$$

$$(10)$$

The sum $P^{(3)}_{10,A} = P^{(3)}_{10,A1} + P^{(3)}_{10,A2}$ contributes to the 3D spectral peak that is situated at ($\omega_\tau = \omega_{10}, \omega_t = \omega_{10}, \omega_T = 0$). This result shows that the peak amplitude is proportional to μ_{10}^4, the peak position reveals the transition frequency, and the peak lineshape profiles in three frequency dimensions are determined by the relaxation rates. Therefore, all parameters in the Hamiltonian matrix elements associated with these two pathways can be extracted from the spectral peak.

The same procedures can be applied to other pathways to calculate the corresponding third-order polarizations. For group B,

$$P^{(3)}_{20,B}(\omega_\tau,\omega_t,\omega_T) = \frac{-iN\mu_{20}^4}{16\sqrt{2}\pi^{\frac{3}{2}}\hbar^3}e^{i\mathbf{k}_S\cdot\mathbf{r}}\mathcal{E}_A^*\mathcal{E}_B\mathcal{E}_C$$

$$\frac{1}{\Gamma_{20}-i(\omega_\tau+\omega_{20})}\cdot\frac{1}{\Gamma_{20}-i(\omega_t-\omega_{20})}$$

$$(\frac{1}{\Gamma_{00}-i\omega_T}+\frac{1}{\Gamma_{22}-i\omega_T}). \qquad (11)$$

For group C,

$$P^{(3)}_{20,C}(\omega_\tau,\omega_t,\omega_T) = \frac{-iN\mu_{10}^2\mu_{20}^2}{16\sqrt{2}\pi^{\frac{3}{2}}\hbar^3}e^{i\mathbf{k}_S\cdot\mathbf{r}}\mathcal{E}_A^*\mathcal{E}_B\mathcal{E}_C$$

$$\frac{1}{\Gamma_{10}-i(\omega_\tau+\omega_{10})}\cdot\frac{1}{\Gamma_{20}-i(\omega_t-\omega_{20})}\cdot\frac{1}{\Gamma_{00}-i\omega_T}.$$

$$(12)$$

For group D,

$$P^{(3)}_{10,D}(\omega_\tau,\omega_t,\omega_T) = \frac{-iN\mu_{10}^2\mu_{20}^2}{16\sqrt{2}\pi^{\frac{3}{2}}\hbar^3}e^{i\mathbf{k}_S\cdot\mathbf{r}}\mathcal{E}_A^*\mathcal{E}_B\mathcal{E}_C$$

$$\frac{1}{\Gamma_{20}-i(\omega_\tau+\omega_{20})}\cdot\frac{1}{\Gamma_{10}-i(\omega_t-\omega_{10})}\cdot\frac{1}{\Gamma_{00}-i\omega_T}.$$
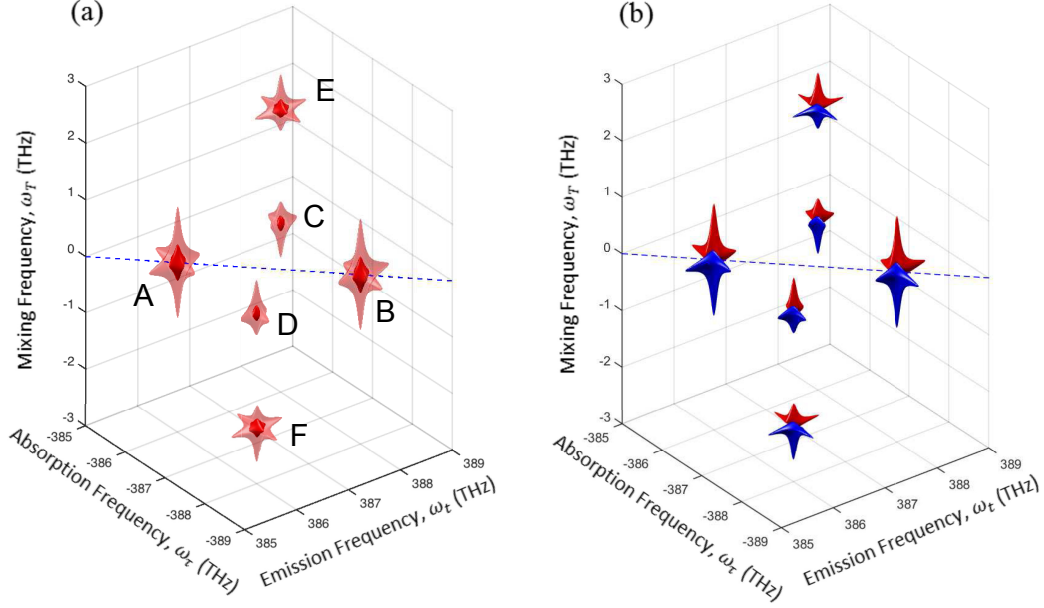
$$(13)$$

For group E,

FIG. 3: Simulated 3D spectra of a three-level V system. (a) The amplitude of the spectrum, where the solid (semi-transparent) red isosurface has a value of 0.3 (0.1) with the maximum amplitude normalized to 1. (b) The real part of the spectrum, where the red (blue) isosurface has a value of 0.1 (-0.1) with the spectrum normalized to a range from -1 to 1.

$$P_{20,E}^{(3)}(\omega_\tau, \omega_t, \omega_T) = \frac{-iN\mu_{10}^2\mu_{20}^2}{16\sqrt{2}\pi^{\frac{3}{2}}\hbar^3}e^{i\mathbf{k}_S\cdot\mathbf{r}}\mathcal{E}_A^*\mathcal{E}_B\mathcal{E}_C$$

$$\frac{1}{\Gamma_{10} - i(\omega_\tau + \omega_{10})} \cdot \frac{1}{\Gamma_{20} - i(\omega_t - \omega_{20})}$$

$$\cdot \frac{1}{\Gamma_{21} - i(\omega_T - \omega_{21})}. \tag{14}$$

For group F,

$$P_{10,F}^{(3)}(\omega_\tau, \omega_t, \omega_T) = \frac{-iN\mu_{10}^2\mu_{20}^2}{16\sqrt{2}\pi^{\frac{3}{2}}\hbar^3}e^{i\mathbf{k}_S\cdot\mathbf{r}}\mathcal{E}_A^*\mathcal{E}_B\mathcal{E}_C$$

$$\frac{1}{\Gamma_{20} - i(\omega_\tau + \omega_{20})} \cdot \frac{1}{\Gamma_{10} - i(\omega_t - \omega_{10})}$$

$$\cdot \frac{1}{\Gamma_{21} - i(\omega_T - \omega_{12})}. \tag{15}$$

Each group results in a spectral peak and there are six separated peaks in the 3D spectrum. The peaks associated with groups A through D have a zero mixing frequency and are located on the plane $\omega_T = 0$. The peaks associated with groups E and F have nonzero mixing frequencies ($\omega_T = \pm\omega_{21}$) and are offset in the ω_T direction.

B. Simulation and interpretation of 3D spectrum

A complete 3D spectrum includes all contributions from Eqs. (9)-(15). The simulated spectra are shown

in Fig. 3, where (a) and (b) show the magnitude and the real part, respectively, of the spectrum. The spectra have three frequency axes ω_τ, ω_t, and ω_T. The spectral peaks are visualized with 3D isosurfaces which are the 3D equivalent to 2D contour lines. For the magnitude, the solid and semi-transparent red surfaces represent the isosurfaces with the values of 0.3 and 0.1, respectively, with the maximum normalized to 1. For the real part, the red and blue surfaces are the isosurfaces with the values of 0.1 and -0.1, respectively, with the spectrum normalized to a range from -1 to 1. The following parameters are used in the simulation: $\omega_{10} = 386$ THz, $\omega_{20} = 388$ THz, $\Gamma_{00} = \Gamma_{11} = \Gamma_{22} = 0.1$ THz, $\Gamma_{10} = \Gamma_{20} = \Gamma_{21} = 0.05$ THz, and $\mu_{10} = \mu_{20}$.

The 3D spectrum has six isolated peaks that can be attributed to the corresponding pathways in Fig. 2(b), as labelled "A-F". Compared to 2D spectra, a 3D spectrum further unfolds the nonlinear optical response in the third dimension ω_T. The off-diagonal peaks in a rephasing 2D spectrum have contributions from two pathways [38]. One of them generates a population during T and does not oscillate, while the other generates a coherence which oscillates during T. In a 3D spectrum, these two contributions have difference frequencies in the ω_T directions and thus are separated. As a result, the contributions from different excitation quantum pathways are well separated in a 3D spectrum. Peaks D-F each corresponds to only a single quantum pathway. Peak A and B each have contributions from two pathways which describe the same process for a closed system. This unique ability to unravel contributions from different excitation

quantum pathways provides a global picture of the non-linear response of a complex system. It also allows separated analyses on each isolated process.
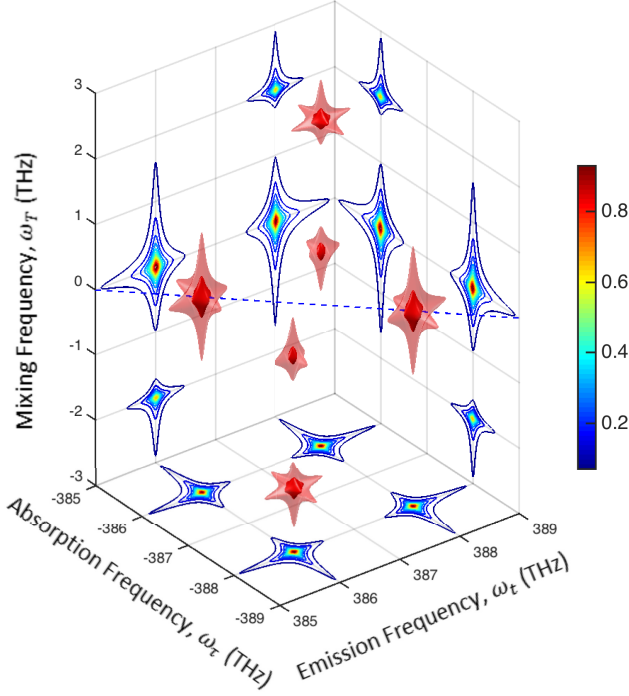

FIG. 4: A 3D spectrum with its 2D projections onto three different 2D planes. Various 2D spectra can be retrieved by projecting a 3D spectrum onto a proper plane.

Various types of 2D spectra can be extracted from a 3D spectrum by projecting it onto the relevant 2D planes. According to the projection-slice theorem of the Fourier-transform [2], the projection of a 3D spectrum onto a 2D plane in the frequency domain is equivalent to a 2D slice in the time domain. As illustrated in Fig. 4, three different types of 2D spectra are obtained by projecting a rephasing 3D spectrum onto three planes. The projection onto the bottom plane (ω_τ, ω_t) is a rephasing one-quantum 2D spectrum $S_I(\omega_\tau, \omega_t)$ at $T = 0$. The 2D spectrum at any given T can be calculated by multiplying the projection with a linear phase term $e^{-i\omega_T T}$, according to the Fourier shift theorem [2]. Similarly, zero-quantum 2D spectra at any given τ can be obtained from the projection onto the left back plane (ω_T, ω_t). These 2D spectra are not unique to 3DCS and can be acquired by 2DCS. However, the projection on the right back plane (ω_T, ω_τ) gives 2D spectra that are not accessible by conventional 2DCS techniques. These 2D spectra reveal the optical response as a function of ω_T and ω_τ at an instantaneous emission time t. In general, a 3D spectrum can be projected onto any planes other than the three planes made of three frequency axes. Such skew projections may have special advantages over standard projections.

By separating contributions from different excitation quantum pathways into isolated 3D peaks, one can now analyze each individual peak to extract the information for single pathways. Here we use peak E in Fig. 3(a) as an example. The peak is carved out from the 3D spectrum and replotted in Fig. 5(a). The projections of this peak onto different 2D planes give 2D spectra of the corresponding single pathway. Some of these 2D spectra cannot be acquired separately for a single pathway in conventional 2DCS. Peak E corresponds to pathway E in Fig. 2(b). The contribution of this pathway is given by Eq. (14). Important parameters in this equation can be extracted from the isolated peak. The strength of the peak is determined by the dipole moments if the number density N is known. Although it is usually difficult to measure the absolute strength of a peak, it is fairly straightforward to compare the peak amplitudes to get the relative strengths of dipole moments. The peak position reveals the transition resonance frequencies ω_{10} and ω_{20}. The relaxation rates Γ_{10}, Γ_{20}, and Γ_{21} are separated in frequency axes ω_τ, ω_t, and ω_T, respectively. As shown in Fig. 5(b-d), slices are taken at the peak in three frequency directions. The slices can be fit to Eq. 14 in separate directions to retrieve the corresponding relaxation rates.

V. INHOMOGENEOUS BROADENING

Inhomogeneous broadening is present in the sample when the resonance frequencies vary within a certain distribution, such as the Doppler broadening in a thermalized atomic vapor, the width variation in a semiconductor quantum well, and the size variation in an ensemble of quantum dots. In conventional 1D spectroscopy, the inhomogeneous broadening often dominates the spectral linewidth, making it challenging to retrieve the homogeneous linewidth. In 2D spectra, homogeneous and inhomogeneous linewidths are unambiguously separated in the cross-diagonal and diagonal directions[5], respectively, providing an easy and robust measurement of both homogenous and inhomogeneous linewidths simultaneously. In this section, we investigate how the inhomogeneous broadening affects the lineshapes in 3D spectra.

The three-level V system, as described above, is discussed here as an example. We assume that both transition frequencies have an inhomogeneous distribution and can be described by a 2D Gaussian distribution as

$$
\begin{aligned}
g(\omega_{10}, \omega_{20}) = & \frac{\sqrt{a_{11}a_{22} - a_{12}^2}}{\pi} \exp\{-[a_{11}(\omega_{10} - \omega_{10}^c)^2 \\
& -2a_{12}(\omega_{10} - \omega_{10}^c)(\omega_{20} - \omega_{20}^c) \\
& +a_{22}(\omega_{20} - \omega_{20}^c)^2]\},
\end{aligned} \tag{16}
$$

where ω_{10}^c and ω_{20}^c are the central frequencies. We define the correlation coefficient

$$
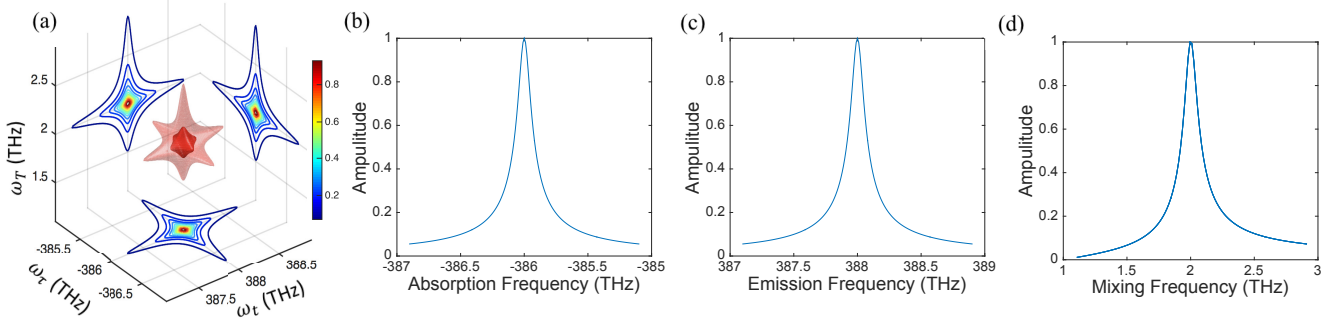R = \frac{a_{12}}{\sqrt{a_{11}a_{22}}} \tag{17}
$$

FIG. 5: (a) An isolated 3D peak with 2D projections. Slices through the peak center along the directions of (b) the absorption frequency ω_τ, (c) the emission frequency ω_t, and (d) the mixing frequency ω_T.

and the linewidths

$$\delta\omega_{10} = \sqrt{\ln 2 \frac{a_{22}}{a_{11}a_{22} - a_{12}^2}}, \tag{18}$$

$$\delta\omega_{20} = \sqrt{\ln 2 \frac{a_{11}}{a_{11}a_{22} - a_{12}^2}}. \tag{19}$$

The third-order polarization can be calculated by integrating the third-order density matrix elements over the 2D Gaussian distribution. For the first diagram in group A in Fig. 2(b), the third-order polarization is given by

$$P_{10,A1}^{(3)}(\tau, t, T)$$
$$= \int_0^\infty d\omega_{10} \int_0^\infty d\omega_{20} g(\omega_{10}, \omega_{20}) N \mu_{10} \rho_{10,A1}^{(3)} e^{i\omega t}. \tag{20}$$

Plug Eqs. (7,16) into this equation and we have

$$P_{10,A1}^{(3)}(\tau, t, T) = \frac{-iN\mu_{10}^4}{8\hbar^3} e^{i\mathbf{k}_S \cdot \mathbf{r}} \mathcal{E}_A^* \mathcal{E}_B \mathcal{E}_C \Theta(\tau)\Theta(T)\Theta(t)$$
$$e^{-\Gamma_{10}(t+\tau) - \Gamma_{00}T} e^{-\frac{1}{4\ln 2}\delta\omega_{10}^2(t-\tau)^2 + i(\omega-\omega_{10}^c)(t-\tau)}. \tag{21}$$

To understand how this term contributes to the spectral line shape, we define new variables $\tau' = t - \tau$ and $t' = t + \tau$ which correspond to the diagonal and cross-diagonal directions, respectively, in the 2D time-domain spectrum. Equation (21) can be rewritten as

$$P_{10,A1}^{(3)}(\tau, t, T) = \frac{-iN\mu_{10}^4}{8\hbar^3} e^{i\mathbf{k}_S \cdot \mathbf{r}} \mathcal{E}_A^* \mathcal{E}_B \mathcal{E}_C \Theta(t' - \tau')\Theta(T)$$
$$\Theta(\tau' + t') e^{-\Gamma_{10}t' - \Gamma_{00}T} e^{-\frac{1}{4\ln 2}\delta\omega_{10}^2\tau'^2 + i(\omega-\omega_{10}^c)\tau'}. \tag{22}$$

In this form, one can intuitively associate the homogeneous linewidths Γ_{10}, Γ_{00}, and the inhomogeneous linewidth $\delta\omega_{10}$ with the t', T, and τ' directions, respectively. However, the homogeneous linewidth Γ_{10} and the inhomogeneous linewidth $\delta\omega_{10}$ are not completely separated along these axes or the corresponding frequency axes because the Θ functions involve t' and τ' in an inseparable way. The Θ functions enforce the causality due to the pulse time ordering and cause the mixing of

homogeneous and inhomogeneous linewidths in the diagonal and cross-diagonal directions. In the strongly homogeneous (inhomogeneous) limit, the homogeneous (inhomogeneous) linewidth can be directly measured from the cross-diagonal (diagonal) slice. However, in the intermediate regime where the homogeneous and inhomogeneous linewidths are comparable, diagonal and cross-diagonal linewidths have mixed contributions from both homogeneous and inhomogeneous broadening. The lineshape in a 2D spectrum with arbitrary homogeneous and inhomogeneous broadening has been analyzed in detail in a previous study [5]. To analyze the lineshape of a 3D spectrum, the spectral response will be calculated in the time domain and numerically Fourier transformed into the frequency domain.

The third-order polarization for other pathways can account for the inhomogeneous broadening in a similar way. For the second pathway in group A, we have

$$P_{10,A2}^{(3)}(\tau, t, T) = \frac{-iN\mu_{10}^4}{8\hbar^3} e^{i\mathbf{k}_S \cdot \mathbf{r}} \mathcal{E}_A^* \mathcal{E}_B \mathcal{E}_C \Theta(\tau)\Theta(T)\Theta(t)$$
$$e^{-\Gamma_{10}(t+\tau) - \Gamma_{11}T} e^{-\frac{1}{4\ln 2}\delta\omega_{10}^2(t-\tau)^2 + i(\omega-\omega_{10}^c)(t-\tau)}. \tag{23}$$

For group B,

$$P_{20,B}^{(3)}(\tau, t, T) = \frac{-iN\mu_{20}^4}{8\hbar^3} e^{i\mathbf{k}_S \cdot \mathbf{r}} \mathcal{E}_A^* \mathcal{E}_B \mathcal{E}_C \Theta(\tau)\Theta(T)\Theta(t)$$
$$e^{-\Gamma_{20}(t+\tau)} \left(e^{-\Gamma_{00}T} + e^{-\Gamma_{22}T} \right)$$
$$e^{-\frac{1}{4\ln 2}\delta\omega_{20}^2(t-\tau)^2 + i(\omega-\omega_{20}^c)(t-\tau)}. \tag{24}$$

For group C,

$$P_{20,C}^{(3)}(\tau, t, T) = \frac{-iN\mu_{10}^2\mu_{20}^2}{8\hbar^3} e^{i\mathbf{k}_S \cdot \mathbf{r}} \mathcal{E}_A^* \mathcal{E}_B \mathcal{E}_C$$
$$\Theta(\tau)\Theta(T)\Theta(t) e^{-\Gamma_{10}\tau - \Gamma_{00}T - \Gamma_{20}t}$$
$$e^{-\frac{1}{4\ln 2}(\delta\omega_{10}^2\tau^2 - 2R\delta\omega_{10}\delta\omega_{20}\tau t + \delta\omega_{20}^2 t^2)} e^{-i(\omega-\omega_{10}^c)\tau + i(\omega-\omega_{20}^c)t}. \tag{25}$$
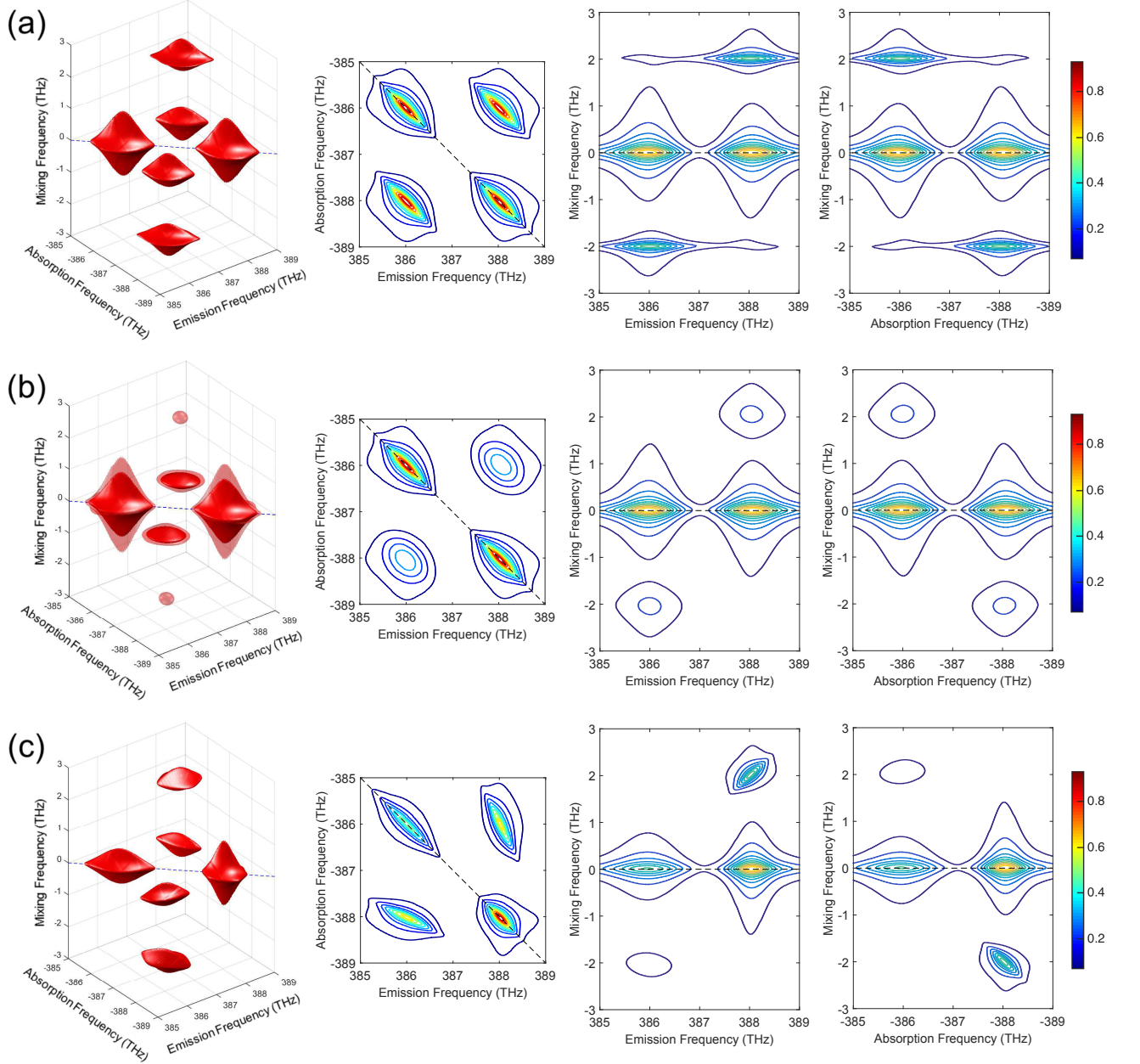
FIG. 6: Simulated 3D spectra of a three-level V system with different inhomogeneous broadening parameters: (a) $R = 1$, $\delta\omega_{10} = \delta\omega_{20} = 0.3$ THz; (b) $R = 0.7$, $\delta\omega_{10} = \delta\omega_{20} = 0.3$ THz; and (c) $R = 1$, $\delta\omega_{10} = 0.4$ THz, $\delta\omega_{20} = 0.2$ THz. The solid (semi-transparent) red isosurface represents a magnitude of 0.1 (0.07) with the maximum normalized to 1. The corresponding 2D projections on the bottom and back planes are also shown for each case.

For group D,

$$P_{10,D}^{(3)}(\tau,t,T) = \frac{-iN\mu_{10}^2\mu_{20}^2}{8\hbar^3}e^{i\mathbf{k}_S\cdot\mathbf{r}}\mathcal{E}_A^*\mathcal{E}_B\mathcal{E}_C$$
$$\Theta(\tau)\Theta(T)\Theta(t)e^{-\Gamma_{20}\tau-\Gamma_{00}T-\Gamma_{10}t}$$
$$e^{-\frac{1}{4\ln 2}(\delta\omega_{20}^2\tau^2-2R\delta\omega_{10}\delta\omega_{20}\tau t+\delta\omega_{10}^2 t^2)}e^{-i(\omega-\omega_{20}^c)\tau+i(\omega-\omega_{10}^c)t}. \tag{26}$$

For group E,

$$P_{20,E}^{(3)}(\tau,t,T) = \frac{-iN\mu_{10}^2\mu_{20}^2}{8\hbar^3}e^{i\mathbf{k}_S\cdot\mathbf{r}}\mathcal{E}_A^*\mathcal{E}_B\mathcal{E}_C$$
$$\Theta(\tau)\Theta(T)\Theta(t)e^{-\Gamma_{10}\tau-\Gamma_{21}T-\Gamma_{20}t}$$
$$e^{-\frac{1}{4\ln 2}[\delta\omega_{10}^2(\tau+T)^2-2R\delta\omega_{10}\delta\omega_{20}(T+\tau)(T+t)+\delta\omega_{20}^2(t+T)^2]}$$
$$e^{-i(\omega-\omega_{10}^c)\tau+i(\omega-\omega_{20}^c)t+i(\omega_{10}^c-\omega_{20}^c)T}. \tag{27}$$

For group F,

$$P_{10,F}^{(3)}(\tau, t, T) = \frac{-iN\mu_{10}^2\mu_{20}^2}{8\hbar^3}e^{i\mathbf{k}_S\cdot\mathbf{r}}\mathcal{E}_A^*\mathcal{E}_B\mathcal{E}_C$$
$$\Theta(\tau)\Theta(T)\Theta(t)e^{-\Gamma_{20}\tau-\Gamma_{21}T-\Gamma_{10}t}$$
$$e^{-\frac{1}{4\ln 2}[\delta\omega_{20}^2(\tau+T)^2-2R\delta\omega_{10}\delta\omega_{20}(T+\tau)(T+t)+\delta\omega_{10}^2(t+T)^2]}$$
$$e^{-i(\omega-\omega_{20}^c)\tau+i(\omega-\omega_{10}^c)t+i(\omega_{20}^c-\omega_{10}^c)T}. \tag{28}$$

The contributions from all pathways are calculated and summed up in the time domain as a function of the three time delays $S_I(\tau, T, t)$. Fourier transforming the signal in all three dimensions generates a 3D spectrum, $S_I(\omega_\tau, \omega_T, \omega_t)$, in the frequency domain. Simulated 3D spectra of an inhomogeneously broadened three-level V system, including the contributions from Eqs. (21~28), are shown in Fig. 6. The first column shows the 3D spectra with 2D Gaussian distribution parameters: (a) $R = 1$, $\delta\omega_{10} = \delta\omega_{20} = 0.3$ THz; (b) $R = 0.7$, $\delta\omega_{10} = \delta\omega_{20} = 0.3$ THz; and (c) $R = 1$, $\delta\omega_{10} = 0.4$ THz, $\delta\omega_{20} = 0.2$ THz. The spectra are normalized to 1 and the magnitude is plotted, where the solid red isosurface has a value of 0.1 and the semi-transparent red isosurface represents 0.07. Other parameters used in the simulation include $\omega_{10} = 386$ THz, $\omega_{20} = 388$ THz, $\Gamma_{00} = \Gamma_{11} = \Gamma_{22} = 0.1$ THz, $\Gamma_{10} = \Gamma_{20} = \Gamma_{21} = 0.05$ THz, and $\mu_{10} = \mu_{20}$. The 2D spectra corresponding to the projections onto planes (ω_τ, ω_t), (ω_T, ω_t), and (ω_T, ω_τ) are also plotted for each 3D spectrum.

If the frequency fluctuations of the two transitions ($|0\rangle \to |1\rangle$ and $|0\rangle \to |2\rangle$) are perfectly correlated ($R = 1$), the inhomogeneous broadening results in an elongation of spectral peak in the diagonal direction ($\omega_\tau = \omega_t$) for the diagonal peaks or in the direction parallel to the diagonal line for the others. The effect is illustrated in Fig. 6(a), where the spectral peaks in both the 3D spectrum and 2D projections are elongated in the corresponding direction. The off-diagonal peaks are associated with both transitions and thus affected by their correlation. If the frequency fluctuations are not fully corrected ($R < 1$), the spectral shape becomes round and the amplitude decreases with the correlation coefficient R for the off-diagonal peaks, as illustrated in the 3D spectrum and 2D projections in Fig. 6(b). The diagonal peaks are not affected by R since they are separately determined by each single transition. In general, the inhomogeneous linewidths of the two transitions may not be equal. The effects of non-equal inhomogeneous linewidths are shown in Fig. 6(c). The diagonal peaks have different linewidths in the diagonal direction. The off-diagonal peaks are tilted compared to the spectra shown in Fig. 6(a). The tilting is more visible in the 2D projections. The projections of the off-diagonal peaks on the (ω_τ, ω_t) plane are tilted with respect to the diagonal direction. The projections on (ω_T, ω_t) and (ω_T, ω_τ) are also tilted in the ω_T direction.

The lineshape of spectral peaks in a 3D spectrum reveals important qualitative information about the inhomogeneous broadening in a system. The presence of inhomogeneous broadening is indicated by the elongation of diagonal peaks. The relative inhomogeneous linewidths of two transitions are revealed by the diagonal linewidth of corresponding diagonal peaks or by the tilting of off-diagonal peaks. The correlation coefficient R is reflected by the roundness of off-diagonal peaks. These parameters R, $\delta\omega_{10}$, and $\delta\omega_{20}$ associated with inhomogeneous broadening can also be quantitatively identified by fitting slices of 3D spectral peaks in proper directions, similar to the approach to fit slices in a 2D spectrum [5].

VI. 3D SPECTRUM OF A THREE-LEVEL LADDER SYSTEM

So far we have discussed 3DCS and its interpretation for a three-level V system with a single ground state and two excited states. The experimental technique and theoretical method can be extended to other systems with different energy-level schemes. Although it works on simpler systems such as isolated homogeneous, inhomogeneous, and heterogenous two-level systems, 3DCS does not have particular advantages in determining the system's nonlinear optical response compared to less sophisticated methods such as 1D linear/nonlinear spectroscopy and 2DCS. However, isolating all quantum pathways in a three-level V system requires 3DCS. A simple extension of a three-level V system is an energy scheme with more than two excited states. A more complicated system may include multiple manifolds of excited states and the transitions of each manifold are dipole allowed. For simplicity, here we consider a three-level ladder system with a ground state, a singly excited state, and a doubly excited state, as shown in Fig. 7(a). The results on this ladder scheme can be generalized to a system with multiple excited states for each manifold.
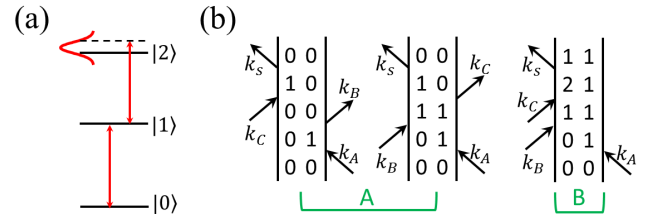

FIG. 7: (a) A three-level ladder system with a singly excited state $|1\rangle$ and a doubly excited state $|2\rangle$. The dash line denotes the double energy of the singly excited state. (b) Double-sided Feynman diagrams representing 3 possible excitation quantum pathways in the experiment.

The excitation pulse sequence in Fig. 1(b) is used to perform 3DCS on a ladder system, as shown in Fig. 7(a), with three states $|0\rangle$, $|1\rangle$, and $|2\rangle$. The transition frequency ω_{21} is slightly lower than the transition frequency ω_{10} by $\Delta\omega = \omega_{21} - \omega_{10}$. The laser wavelength is tuned to be on resonance with the $|1\rangle \to |0\rangle$ and the double frequency covers the state $|2\rangle$. The TFWM signal in
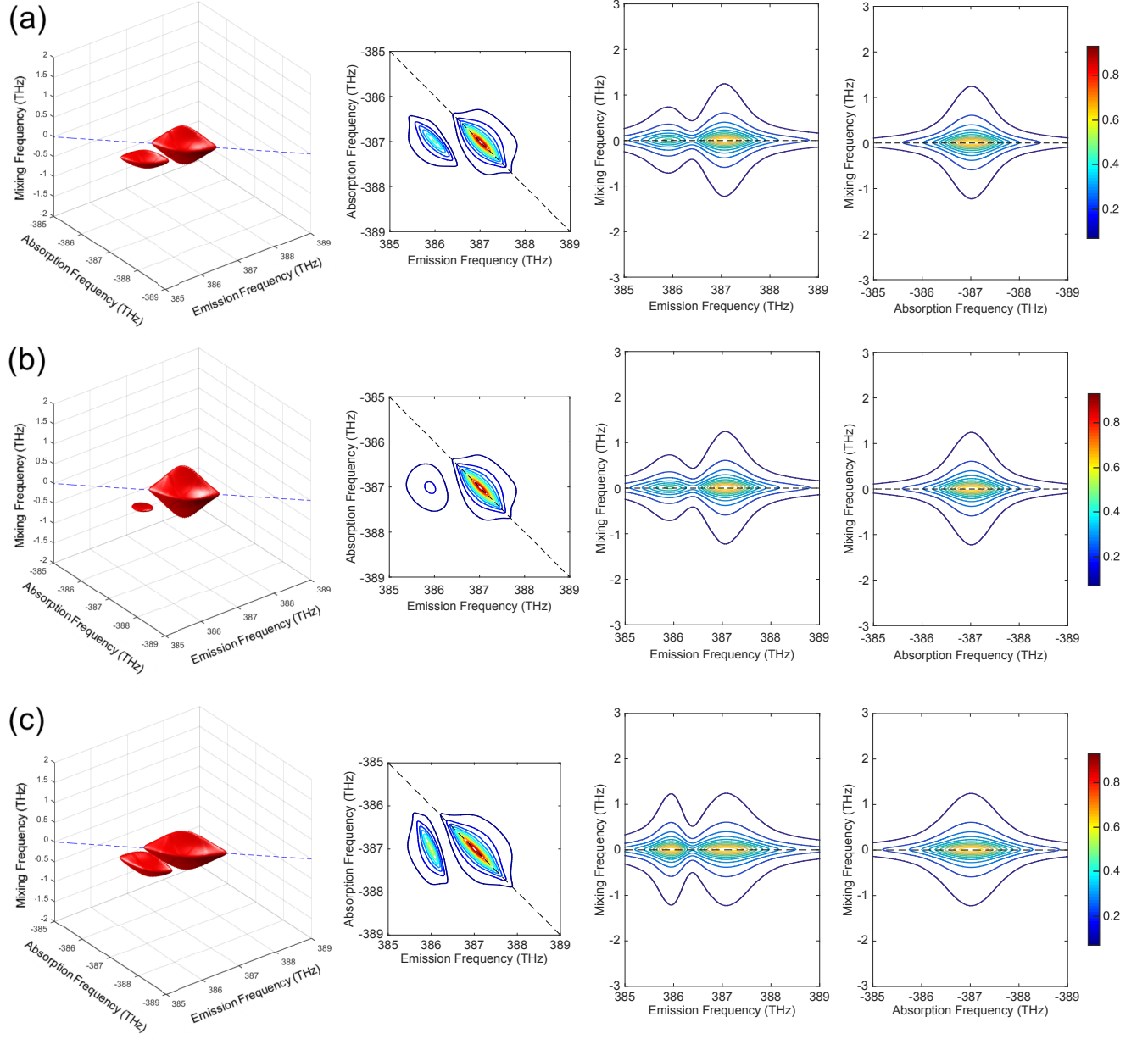
FIG. 8: Simulated 3D spectra of a three-level ladder system with different inhomogeneous broadening parameters: (a) $R = 1$, $\delta\omega_{10} = \delta\omega_{21} = 0.3$ THz; (b) $R = 0.7$, $\delta\omega_{10} = \delta\omega_{21} = 0.3$ THz; and (c) $R = 1$, $\delta\omega_{10} = 0.4$ THz, $\delta\omega_{21} = 0.2$ THz. The solid red isosurface represents a magnitude of 0.2 with the maximum normalized to 1. The corresponding 2D projections on the bottom and back planes are also shown for each case.

the phase matched direction, $\mathbf{k}_s = -\mathbf{k}_A + \mathbf{k}_B + \mathbf{k}_C$, has contributions from three excitation pathways shown in Fig. 7(b). The pathways in group A are the same as the ones in Fig. 2(b), involving only states $|0\rangle$ and $|1\rangle$. This group gives rise to a diagonal peak. The pathway in group B involves the doubly excited state $|2\rangle$, resulting in a peak with an absorption frequency ω_{10} and an emission frequency ω_{21}. To account for the inhomogeneous broadening, we use a 2D Gaussian distribution to describe the inhomogeneous broadening of the two transitions and their correlation,

$$
\begin{aligned}
g(\omega_{10}, \omega_{21}) = {} & \frac{\sqrt{a_{11}a_{22} - a_{12}^2}}{\pi} \exp\{-[a_{11}(\omega_{10} - \omega_{10}^c)^2 \\
& - 2a_{12}(\omega_{10} - \omega_{10}^c)(\omega_{21} - \omega_{21}^c) \\
& + a_{22}(\omega_{21} - \omega_{21}^c)^2]\},
\end{aligned}
\tag{29}
$$

where ω_{10}^c and ω_{21}^c are the central frequencies. The cor-

relation coefficient is defined as

$$R = \frac{a_{12}}{\sqrt{a_{11}a_{22}}}. \qquad (30)$$

The linewidths are defined as

$$\delta\omega_{10} = \sqrt{\ln 2 \frac{a_{22}}{a_{11}a_{22} - a_{12}^2}}, \qquad (31)$$

$$\delta\omega_{21} = \sqrt{\ln 2 \frac{a_{11}}{a_{11}a_{22} - a_{12}^2}}. \qquad (32)$$

The third-order polarization due to the pathways in group A can be calculated as Eqs. (21, 23). The contribution by group B is

$$P_{21,B}^{(3)}(\tau,t,T) = \frac{iN\mu_{10}^2\mu_{21}^2}{8\hbar^3} e^{i\mathbf{k}_S\cdot\mathbf{r}} \mathcal{E}_A^* \mathcal{E}_B \mathcal{E}_C \Theta(\tau)\Theta(T)\Theta(t)$$
$$e^{-\Gamma_{10}\tau - \Gamma_{11}T - \Gamma_{21}t} e^{-\frac{1}{4\ln 2}(\delta\omega_{10}^2\tau^2 - 2R\delta\omega_{10}\delta\omega_{21}\tau t + \delta\omega_{21}^2 t^2)}$$
$$e^{-i(\omega - \omega_{10}^c)\tau + i(\omega - \omega_{21}^c)t}. \qquad (33)$$

The overall TFWM signal can be calculated in the time domain using Eqs. (21, 23, 33). Fourier transforming the time-domain signal generates a 3D spectrum in the frequency domain. Simulated 3D spectra of the ladder system are shown in Fig. 8. The first column shows the 3D spectra with the 2D Gaussian distribution parameters: (a) $R = 1$, $\delta\omega_{10} = \delta\omega_{21} = 0.3$ THz; (b) $R = 0.7$, $\delta\omega_{10} = \delta\omega_{21} = 0.3$ THz; and (c) $R = 1$, $\delta\omega_{10} = 0.4$ THz, $\delta\omega_{21} = 0.2$ THz. The magnitude of the spetra is plotted. The shown isosurface has a value of 0.2 with the maximum amplitude normlized to 1. The corresponding 2D projections onto three planes are also shown for each 3D spectrum. Other parameters used in the simulation are $\omega_{10} = 387$ THz, $\omega_{21} = 386$ THz, $\Gamma_{00} = \Gamma_{11} = 0.1$ THz, $\Gamma_{10} = \Gamma_{21} = 0.05$ THz, and $\mu_{10} = \mu_{21}$.

The 3D spectra have a peak on the diagonal line. This peak is contributed only by the $|1\rangle \rightarrow |0\rangle$ transition and not related to the doubly excited state $|2\rangle$. The off-diagonal peak is contributed by pathway B in Fig. 7(b) and involves the doubly excited state $|2\rangle$. This peak has an absoprtion frequency of ω_{10} and an emission frequency of ω_{21}. The energy difference between the upper and lower transitions can be easily measured in a 3D spectrum or its projection on the bottom plane, while it may be difficult in 1D spectra with the presense of inhomogeneous broadening. This energy difference can reveal important information about the system, for example, the binding energy of biexcitons if the doubly excited state represents a biexciton state. The lineshape of the diagonal peak is affected by the inhomogeneous broadening of the lower transition alone. However, the off-diagonal peak is affected by the inhomogeneous broadenings of both transitions and their correlation. As shown in Fig. 8(a), when the correlation coeficient R is 1 and both inhomogeneous linewidths are the same, the off-diagonal and diagonal peaks are elongated similarly in a direction

that is parallel to the diagonal direction. As the correlation coeficient R decreases, the off-diagonal peak becomes round in lineshape and weaker in relative amplitude, as shown in Fig. 8(b). If the inhomogeneous linewidths of the two transitions are not equal while $R = 1$, the long axis of the off-diagonal peak is tilted relative to the diagonal line, as shown in Fig. 8(c). The effects of different 2D Gaussian distribution parameters are clearly shown in the 2D projection on the bottom plane (ω_τ, ω_t), while the differences are not visible in the projections on the two back planes (ω_T, ω_t) and (ω_T, ω_τ).

Quantitative information about the ladder system can be retrieved by analyzing 3D spectra. The peak positions reveal the central frequencies of the upper and lower transitions. The lineshape analysis can provide information of homogeneous linewidths, as well as the parameters in the 2D Gaussian distribution of inhomogeneous broadening.

VII. SUMMARY

Based on the optical Bloch equations, we calculated the third-order nonlinear optical responses to a given excitation pulse sequence in a particular phase matching direction, and generated 3D spectra of three different systems including a three-level V system with and without inhomogeneous broadening, and an inhomogeneous three-level ladder system. The simulated 3D spectra have features that can be related to specific aspects of the system's nonlinear optical response. Quantitative values of important parameters can be extracted from the spectral pattern, peak positions, amplitudes, and line shapes. Following a similar strategy, 3D spectra of more sophisticated systems, some of which may be considered as a generalization or combination of the three examples, can be analyzed by using an optical Bloch equation based model to extract quantitative information of interest. Understanding how different properties of the system are manifested in 3D spectra helps to develop a general approach to interpret 3D spectra, and to identify more systems/problems where 3DCS has advantages over 2D/1D techniques.

Acknowledgments

Appendix: Double-sided Feynman diagrams

The perturbative solution of optical Bloch equations may consist of multiple terms corresponding to different excitation quantum pathways. Each term can be represented conveniently by using the so-called double-sided Feynman diagram. In this appendix, we introduce the

conventions used in this article regarding double-sided Feynman diagrams.

A double-sided Feynman diagram tracks the time evolution of the density matrix elements. The diagrams use two vertical lines with two symbols in between to represent the "bra" and "ket" of the density matrix operator, where the left (right) line represents the "ket" ("bra"). The time increases upward. The interaction with a field is described by the vertex of an arrow with a vertical line. An arrow represents a field that can change one side of the density matrix element. An arrow pointing to the right indicates the field has the form $\hat{E}_n \exp(i\mathbf{k}_n \cdot \mathbf{r} - i\omega_n t)$, while an arrow pointing to the left implies the field is conjugated, with the form $\hat{E}_n^* \exp(-i\mathbf{k}_n \cdot \mathbf{r} + i\omega_n t)$. If the arrow points towards (away from) the vertical lines, a photon is absorbed (emitted) and drives the density matrix element from a lower (higher) energy state to a higher (lower) energy state.
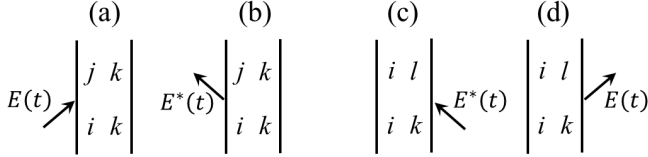

FIG. 9: Four possible types of vertices in double-sided Feynman diagrams.

There are four possible vertices, as shown in Fig. 9(a-d). Each one describes the time evolution from the $(n-1)^{th}$ order density matrix element $\rho_{ik}^{(n-1)}$ to the nth order density matrix element $\rho_{jk}^{(n-1)}$ or $\rho_{il}^{(n-1)}$. The nth order density matrix element is determined by the $(n-1)^{th}$ order density matrix element, the energy separation and the dipole moment of the transition, the de-

cay and dephasing rates, and the excitation field. For the four vertices, the nth order density matrix element can be calculated using the following integrals accordingly,

$$
\text{(a)} \quad \rho_{jk}^{(n)} = \frac{i\mu_{ij}}{2\hbar} e^{i\mathbf{k}_n \cdot \mathbf{r}} \int_{-\infty}^{t} \hat{E}_n(t') e^{-i\omega_n t'}
$$
$$
e^{-i\Omega_{jk}(t-t')} \rho_{ik}^{(n-1)}(t') dt', \quad \text{(A.1)}
$$

$$
\text{(b)} \quad \rho_{jk}^{(n)} = \frac{i\mu_{ij}}{2\hbar} e^{-i\mathbf{k}_n \cdot \mathbf{r}} \int_{-\infty}^{t} \hat{E}_n^*(t') e^{i\omega_n t'}
$$
$$
e^{-i\Omega_{jk}(t-t')} \rho_{ik}^{(n-1)}(t') dt', \quad \text{(A.2)}
$$

$$
\text{(c)} \quad \rho_{il}^{(n)} = -\frac{i\mu_{kl}}{2\hbar} e^{-i\mathbf{k}_n \cdot \mathbf{r}} \int_{-\infty}^{t} \hat{E}_n^*(t') e^{i\omega_n t'}
$$
$$
e^{-i\Omega_{il}(t-t')} \rho_{ik}^{(n-1)}(t') dt', \quad \text{(A.3)}
$$

$$
\text{(d)} \quad \rho_{il}^{(n)} = -\frac{i\mu_{kl}}{2\hbar} e^{i\mathbf{k}_n \cdot \mathbf{r}} \int_{-\infty}^{t} \hat{E}_n(t') e^{-i\omega_n t'}
$$
$$
e^{-i\Omega_{il}(t-t')} \rho_{ik}^{(n-1)}(t') dt', \quad \text{(A.4)}
$$

where $\Omega_{ij} = \omega_i - \omega_j - i\Gamma_{ij}$.

Each doubled-sided Feynman diagram containing one vertex describes one order in the perturbation expansion. The nth order perturbation solution of a density matrix element can be represented by a diagram with n vertices stacked up vertically. Using the above integrals, the nth order density matrix element can be calculated from the $(n-1)^{th}$ order which can in turn be calculated from a lower order component. This process is repeated until the lower order density matrix element is given by the initial condition. This method is used in this article to calculate the high order component for each double-sided Feynman diagram.

[1] S. T. Cundiff and S. Mukamel, Phys. Today **66**, 44 (2013).
[2] R. Ernst, G. Bodenhausen, and A. Wokaun, *Principles of Nuclear Magnetic Resonance in One and Two Dimensions* (Oxford Science Publications, Oxford, U.K., 1987).
[3] D. M. Jonas, Annu. Rev. Phys. Chem. **54**, 425 (2003).
[4] H. Li and S. T. Cundiff, Adv. At., Mol., Opt. Phys. **66**, 1 (2017).
[5] M. E. Siemens, G. Moody, H. Li, A. D. Bristow, and S. T. Cundiff, Opt. Express **18**, 17699 (2010).
[6] P. Hamm, M. Lim, W. F. DeGrado, and R. M. Hochstrasser, Proc. Natl. Acad. Sci. U.S.A. **96**, 2036 (1999).
[7] C. J. Fecko, J. D. Eaves, J. J. Loparo, A. Tokmakoff, and P. L. Geissler, Science **301**, 1698 (2003).
[8] T. Brixner, J. Stenger, H. M. Vaswani, M. Cho, R. E. Blankenship, and G. R. Fleming, Nature **434**, 625 (2005).
[9] G. S. Engel, T. R. Calhoun, E. L. Read, T.-K. Ahn, T. Mancal, Y.-C. Cheng, R. E. Blankenship, and G. R. Fleming, Nature **446**, 782 (2007).
[10] E. Collini, C. Y. Wong, K. E. Wilk, P. M. G. Curmi, P. Brumer, and G. D. Scholes, Nature **463**, 644 (2010).
[11] X. Dai, M. Richter, H. Li, A. D. Bristow, C. Falvo, S. Mukamel, and S. T. Cundiff, Phys. Rev. Lett. **108**, 193201 (2012).
[12] F. Gao, S. T. Cundiff, and H. Li, Opt. Lett. **41**, 2954 (2016).
[13] G. Nardin, G. Moody, R. Singh, T. M. Autry, H. Li, F. Morier-Genoud, and S. T. Cundiff, Phys. Rev. Lett. **112**, 046402 (2014).
[14] R. Singh, T. M. Autry, G. Nardin, G. Moody, H. Li, K. Pierz, M. Bieler, and S. T. Cundiff, Phys. Rev. B **88**, 45304 (2013).
[15] D. Turner, P. Wen, D. Arias, K. Nelson, H. Li, G. Moody, M. Siemens, and S. Cundiff, Phys. Rev. B **85**, 201303 (2012).
[16] S. T. Cundiff, A. D. Bristow, M. Siemens, H. Li, G. Moody, D. Karaiskaj, X. Dai, and T. Zhang, IEEE J. Select. Topics Quantum Electron. **18**, 318 (2012).
[17] G. Moody, I. A. Akimov, H. Li, R. Singh, D. R. Yakovlev,

G. Karczewski, M. Wiater, T. Wojtowicz, M. Bayer, and S. T. Cundiff, Phys. Rev. Lett. **112**, 97401 (2014).

[18] G. Moody, R. Singh, H. Li, I. A. Akimov, M. Bayer, D. Reuter, A. D. Wieck, A. S. Bracker, D. Gammon, and S. T. Cundiff, Phys. Status Solidi **250**, 1753 (2013).

[19] G. Moody, R. Singh, H. Li, I. A. Akimov, M. Bayer, D. Reuter, A. D. Wieck, A. S. Bracker, D. Gammon, and S. T. Cundiff, Phys. Rev. B **87**, 41304 (2013).

[20] G. Moody, R. Singh, H. Li, I. A. Akimov, M. Bayer, D. Reuter, A. D. Wieck, and S. T. Cundiff, Solid State Commun **163**, 65 (2013).

[21] G. Moody, R. Singh, H. Li, I. A. Akimov, M. Bayer, D. Reuter, A. D. Wieck, and S. T. Cundiff, Phys. Rev. B **87**, 045313 (2013).

[22] S. T. Cundiff, Phys. Chem. Chem. Phys. **16**, 8193 (2014).

[23] F. Ding and M. T. Zanni, Chem. Phys. **341**, 95 (2007).

[24] S. S. Mukherjee, D. R. Skoff, C. T. Middleton, and M. T. Zanni, J. Chem. Phys. **139**, 144205 (2013).

[25] S. Garrett-Roe and P. Hamm, J. Chem. Phys. **130**, 164510 (2009).

[26] S. Garrett-Roe, F. Perakis, F. Rao, and P. Hamm, J. Phys. Chem. B **115**, 6976 (2011).

[27] A. F. Fidler, E. Harel, and G. S. Engel, J. Phys. Chem. Lett. **1**, 2876 (2010).

[28] D. B. Turner, K. W. Stone, K. Gundogdu, and K. A. Nelson, J. Chem. Phys. **131**, 144510 (2009).

[29] J. A. Davis, C. R. Hall, L. V. Dao, K. A. Nugent, H. M. Quiney, H. H. Tan, and C. Jagadish, J. Chem. Phys. **135**, 044510 (2011).

[30] H. Li, A. D. Bristow, M. E. Siemens, G. Moody, and S. T. Cundiff, Nat. Commun. **4**, 1390 (2013).

[31] D. Hayes and G. Engel, Biophys. J. **100**, 2043 (2011).

[32] P. C. Chen, T. a. Wells, and B. R. Strangfeld, J. Phys. Chem. A **117**, 5981 (2013).

[33] A. D. Bristow, D. Karaiskaj, X. Dai, and S. T. Cundiff, Opt. Express **16**, 18017 (2008).

[34] H. Li, G. Moody, and S. T. Cundiff, Opt. Express **21**, 1687 (2013).

[35] H. Li, A. P. Spencer, A. Kortyna, G. Moody, D. M. Jonas, and S. T. Cundiff, J. Phys. Chem. A **117**, 6279 (2013).

[36] A. P. Spencer, H. Li, S. T. Cundiff, and D. M. Jonas, J. Phys. Chem. A **119**, 3936 (2015).

[37] M. O. Scully and M. S. Zubairy, *Quantum Optics* (Cambridge University Press, 1997).

[38] X. Dai, A. D. Bristow, D. Karaiskaj, and S. T. Cundiff, Phys. Rev. A **82**, 52503 (2010).